Journal of Materials Chemistry A

ROYAL SOCIETY OF CHEMISTRY

PAPER

View Article Online
View Journal | View Issue

Cite this: J. Mater. Chem. A, 2024, 12, 11390

Effects of sulfate modification of stoichiometric and lithium-rich $LiNiO_2$ cathode materials†

Bo Dong, *[ad] Andrey D. Poletayev, [bd] Jonathon P. Cottom, [bdgh] Javier Castells-Gil, [ad] Ben F. Spencer, [e] Cheng Li,[f] Pengcheng Zhu, [cd] Yongxiu Chen, [cd] Jaime-Marie Price, [ad] Laura L. Driscoll,[ad] Phoebe K. Allan, [ad] Emma Kendrick, [cd] M. Saiful Islam *[bdg] and Peter R. Slater *[ad]

Received 12th January 2024
Accepted 3rd April 2024

DOI: 10.1039/d4ta00284a

rsc.li/materials-a

Lithium nickel oxide, $LiNiO_2$, has attracted considerable interest as a high energy cathode for next generation lithium-ion batteries. Nevertheless, shortcomings such as significant cycling capacity decay and low stability in ambient atmosphere have hindered its practical application, and consequently most work has focused on the more stable Mn and Co doped analogues $Li(Ni,Mn,Co)O_2$. Here, we report an investigation of an alternative strategy, sulfate modification, in the $LiNiO_2$ system. We show that improved performance can be achieved, attributed to the dual effect of a low level of bulk doping and the presence of a self-passivation Li_2SO_4 layer formed beyond the solid solution limit. *Ab initio* simulations suggest that the behavior is similar to that of other high valent dopants such as W and Mo. These dual effects contribute to the improved air stability and enhanced electrochemical performance for the sulfate modified lithium-rich $LiNiO_2$, leading to high initial capacities (~245 mA h g^{-1} at 25 mA g^{-1}, and ~205 mA h g^{-1} at 100 mA g^{-1}) and better capacity retention. Overall, the results show that polyanion modification represents an excellent alternative low-cost strategy to improve the performance of lithium nickel oxide cathode materials.

1. Introduction

Lithium-ion batteries (LIBs) dominate the energy storage market for portable electronics and electrical vehicles (EVs) due to their high energy densities.[1–4] Ni-rich lithium transition metal oxides, such as $LiNi_xCo_yAl_{1-x-y}O_2$ (NCA) and $LiNi_xMn_yCo_{1-x-y}O_2$ (NMC) have attracted great interest and are extensively applied in the field.[5–7] However, the high and volatile cost of Co hinders their long-term sustainability and motivates research into higher Ni content, lower Co content NMC (NMC811, $LiNi_{0.8}Mn_{0.1}Co_{0.1}O_2$) materials. Ultimately a key aim is to eliminate Co to give $LiNiO_2$ (LNO), which is considered as the promising next generation cathode due to its high theoretical capacity of ~270 mA h g^{-1} and high average voltage of 3.8 V *vs.* Li metal.[8,9]

However, the intrinsic problems with this stoichiometric LNO phase, such as moisture instability at ambient atmosphere, detrimental phase transitions and particle cracking at high states of charge remain unresolved.[10,11] During delithiation, several phase transitions of $Li_{1-x}NiO_2$ occur during the charging process, which includes hexagonal (H1, $0 \le x \le 0.25$) to monoclinic (M, $0.25 \le x \le 0.55$), monoclinic (M) to hexagonal (H2, $0.55 \le x \le 0.75$), and hexagonal (H2) to hexagonal (H3, $0.75 \le x \le 1$).[12–15] In particular, the H2–H3 phase transition of $Li_{1-x}NiO_2$ above 4.1 V triggers the shrinkage of the unit cell and large volume change due to the large difference of c parameters of H2 (c = 14.404(1) Å) and H3 (c = 13.363(6) Å) phases.[16,17] The resulting microcracks of active cathode material leads to further side reactions of cathode and electrolyte, which accelerates the capacity fade of $LiNiO_2$.[18] To mitigate these issues, most attempts have focused on dopant incorporation and surface modification to stabilise the material.[19–22]

It has been demonstrated that Ti or Zr doped $LiNiO_2$ have limited solid solution ranges, with a small amount of dopant incorporation into the bulk structure and with the remaining dopant forming surface layers (such as Li_2TiO_3 and Li_2ZrO_3) on

[a]School of Chemistry, University of Birmingham, Birmingham B15 2TT, UK. E-mail: b.dong@bham.ac.uk; p.r.slater@bham.ac.uk
[b]Department of Materials, University of Oxford, Oxford, OX1 3PH, UK. E-mail: Saiful.islam@materials.ox.ac.uk
[c]School of Metallurgy and Materials, University of Birmingham, Birmingham B15 2TT, UK
[d]The Faraday Institution, Harwell Science and Innovation Campus, Didcot OX11 0RA, UK
[e]Department of Materials and Henry Royce Institute, The University of Manchester, Oxford Road, Manchester, M13 9PL, UK
[f]Neutron Sciences Directorate, Spallation Neutron Source (SNS), Oak Ridge National Laboratory, 37830, TN, USA
[g]Department of Chemistry, University of Bath, Bath, BA2 7AY, UK
[h]Leiden Institute of Chemistry, Gorlaeus Laboratories, Leiden University, 2300 RA Leiden, The Netherlands

† Electronic supplementary information (ESI) available. See DOI: https://doi.org/10.1039/d4ta00284a

the $LiNiO_2$ particles.[23,24] In other work, Al or Mg doping of $LiNiO_2$ was found to dramatically reduce the amount of residual surface lithium carbonate in ambient atmosphere owing to strong TM(Al/Mg)–O bonding, which inhibits the reaction between water/carbon dioxide and $LiNiO_2$.[25–27] High-valence dopants, such as W and Mo, have also been examined in $LiNiO_2$.[28–32] *In situ* XRD results have indicated that W doped $LiNiO_2$ modified the H2–H3 phase transition into a more gradual solid solution reaction during cycling, and the resulting enhancement of cycling stability was attributed to an alleviation of the structural stress and abrupt lattice changes.[28]

All these previous studies have involved doping with cations of similar octahedral size to Ni. As an alternative to such cation incorporation, polyanion doping is a less widely used strategy in altering the structural, chemical or physical properties of inorganic materials. This methodology has attracted much interest in perovskite oxide electrodes for solid oxide fuel cells, where results illustrate that transition-metal octahedra TMO_6 can be replaced with tetrahedral MO_4 (M = Si, S, P) or trigonal planar MO_3 (C, B) to create materials with improved properties.[33–41]

In this work, we examine the effect of sulfate modification in $LiNiO_2$ and Li-rich $LiNiO_2$, and the corresponding effect on the structural and electrochemical properties using a combined experimental and modelling approach. The formation of Li-rich phases with Ni-rich compositions has been challenging so far, producing poorly ordered materials. The aim of polyanion doping was also to introduce tetrahedral ions with higher charge and oxygen vacancies in order to help to stabilise a Li-rich phase that is otherwise challenging to isolate.[42] Our results show enhanced electrochemical performance on sulfate incorporation compared to undoped materials prepared under comparable conditions.

2. Results and discussion

2.1 Phase formation and crystal structures

2.1.1 X-ray/neutron diffraction and spectroscopy. We first investigated the incorporation of the polyanion dopant, SO_4^{2-}, in Li-stoichiometric $LiNiO_2$ (LNO). $LiNiO_2$ and sulfate doped $LiNi_{1-x}S_xO_{2-\delta}$, were initially made *via* the conventional solid state route at 700–725 °C/12 h in O_2. As shown in Fig. 1, the XRD patterns of sulfate doped $LiNiO_2$ show a single layered phase for $x = 0.025$. As shown in Table 1, the cell volume of sulfate doped $LiNiO_2$ increased compared to that of the undoped sample, which is consistent with the suggested partial reduction in line with prior work on sulfate doped perovskite systems. The intensity ratio I_{003}/I_{104} between the (003) and (104) reflections has been intensively used in LNO as an indicator of the Li/Ni antisites defect: the higher the I_{003}/I_{104} ratio, indicates a more perfect layered $LiNiO_2$ structure without anti-site disorder. Sulfate doped samples indeed show an increase in the I_{003}/I_{104} ratio (Table 2), which suggests improved structural ordering in the material.

Following these initial results and given that the doping was expected to lower the anion content (total anion charge), and the dopant (normally S^{6+}) has a higher charge than Ni, the possible stabilisation of higher Li content/lower Ni content phases was investigated. Sulfate doped Li-rich $LiNiO_2$ (S-LRNO)

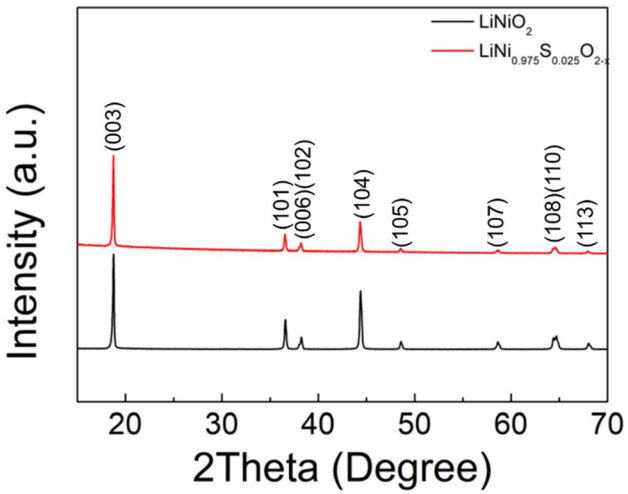

Fig. 1 XRD patterns of $LiNiO_2$ and S doped $LiNiO_2$ (solid state synthesis route).

Table 1 Cell parameters of polyanion doped $LiNiO_2$

Composition	$a = b$ (Å)	c (Å)	V (Å^3)
$LiNiO_2$	2.8814(1)	14.2079(1)	102.16(2)
$LiNi_{0.975}S_{0.025}O_{2-x}$	2.8817(1)	14.2155(1)	102.23(2)

Table 2 I_{003}/I_{104} of polyanion doped $LiNiO_2$

Composition	I_{003}/I_{104}
$LiNiO_2$	1.569
$LiNi_{0.975}S_{0.025}O_{2-x}$	2.834

were made under similar conditions used for LNO to increase the capacity. As shown in Fig. 2a (XRD data), the S-free control $Li_{1.1}Ni_{0.85}O_2$ shows a majority layered phase with unknown impurity peaks at lower two theta angles. In contrast, when adding a small amount of sulfate, $Li_{1.1}Ni_{0.875}S_{0.025}O_{2-\delta}$ shows a single-phase sample, indicating the benefits of sulfate in stabilising the phase formation. A small amount of Li_2SO_4 impurity was detected with increasing sulfate content ($Li_{1.1}Ni_{0.85}S_{0.05}O_{2-\delta}$), suggesting only a low-level incorporation of sulfate in the Li-rich $LiNiO_2$ system. The presence of a small amount of bulk sulfate and a surface Li_2SO_4 layer for this sample is supported by the XPS/HAXPES data (see later).

Structural refinement of $Li_{1.1}Ni_{0.85}S_{0.05}O_{2-\delta}$ using neutron diffraction data was performed, with the profile fits shown in Fig. 2b. Weight fractions of Li_2SO_4, Li_2CO_3 and $Li_{1.1}Ni_{0.85}S_{0.05}O_{2-\delta}$ were refined to give 95.9% S-LRNO, 2.0% Li_2SO_4 and 2.1% Li_2CO_3, which is consistent to XRD results. 0.03 S was then added to the Li2/Ni2 site (Ni layer), and constraints of the same U_{iso} and full occupancy were made for Li1/Ni1; and Li2/Ni2/S1. The atomic position of O1 was refined followed by U_{isos} of all atoms which were fixed after convergency. The occupancies of Li1/Ni1, Li2/Ni2 (to give the occupancy of S1) and O1 were refined. A final refinement of the U_{iso} of all atoms showed only a small change

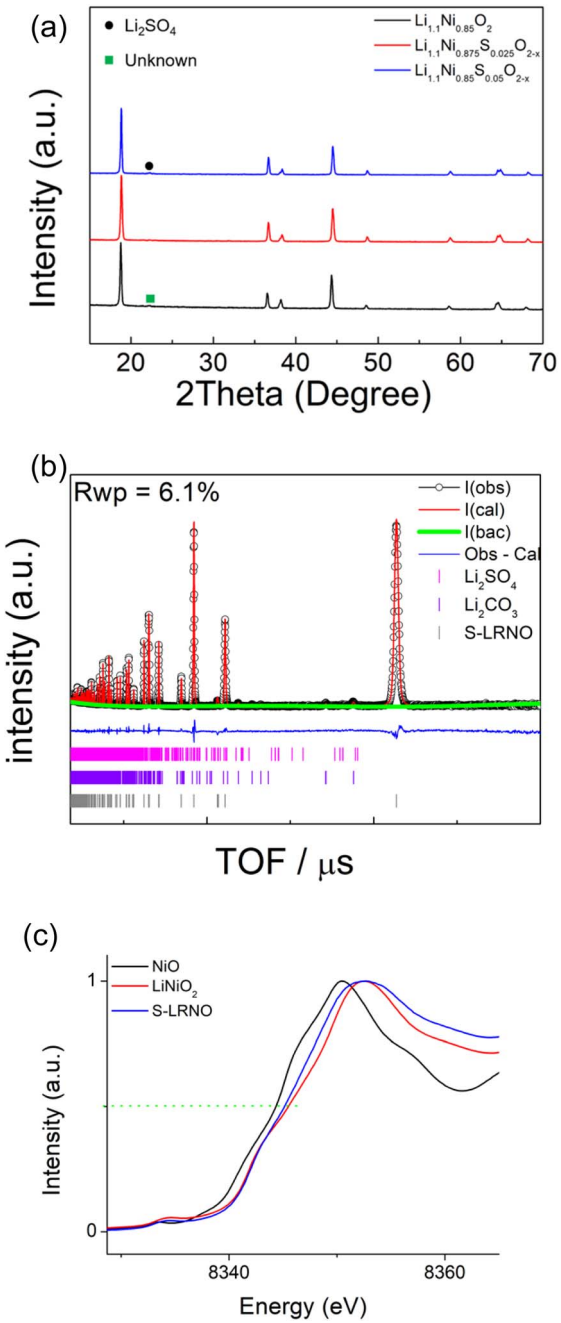

Fig. 2 (a) XRD patterns of $Li_{1.1}Ni_{0.85}O_2$, $Li_{1.1}Ni_{0.875}S_{0.025}O_{2-x}$ and $Li_{1.1}Ni_{0.85}S_{0.05}O_{2-x}$ (solid state synthesis route). (b) Observed, calculated and difference profiles from structural refinement of $Li_{1.1}Ni_{0.85}S_{0.05}O_{2-\delta}$ using neutron diffraction data (c) XAS data of $Li_{1.1}Ni_{0.85}S_{0.05}O_{2-x}$.

and the final parameters are shown in Table 3. From these data, the refined composition was determined to be $Li_{1.047(3)}Ni_{0.922(3)}S_{0.031}O_{1.98(2)}$, consistent with the formation of a higher Li content/lower Ni content phase.

In support of sulfate doping, the Ni K-edge XAS also indicates a small shift for the sulfate doped sample, where the normalised absorption of S-LRNO is shifted to lower energy compared to that of $LiNiO_2$ (Fig. 2c). The slight shift of the Ni K-edge for S-LRNO suggests the partial reduction of Ni^{3+} in the bulk material. In order to evaluate the surface states, XPS data were collected. Here, the Ni 2p spectrum (Fig. S1†) is dominated by the spin–orbit doublet characterized by binding energies of the Ni $2p_{3/2}$ and Ni $2p_{1/2}$ core levels of 855.2 and 872.6 eV, respectively. The spectra also show broad satellites at 862.7 and 879.2 eV. All of these binding energy values are representative of the nickel environments in $LiNiO_2$.[43,44]

Table 3 Structural parameters of $Li_{1.1}Ni_{0.85}S_{0.05}O_{2-x}$ from Rietveld refinement using neutron diffraction data[a]

Atom	x	y	z	Mult.	Occupancy	U_{iso} (Å^2)
Li1	0	0	0	3	0.978(2)	0.016
Ni1	0	0	0	3	0.022(2)	0.016
S1	0	0	0.5	3	0.031	0.002
Li2	0	0	0.5	3	0.069(1)	0.002
Ni2	0	0	0.5	3	0.900(1)	0.002
O1	0	0	0.242(1)	6	0.992(4)	0.011

[a] Space group: $R\bar{3}mh$, $a = b = 2.8777(1)$ Å, $c = 14.1938(1)$ Å, $V = 101.79(1)$ Å^3.

HAXPES and XPS spectra were collected to investigate the presence of S dopant in the bulk and on the surface of S-LNRO, respectively. XPS and HAXPES spectra of S 2p of S-LRNO are shown in Fig. 3a and b. The S 2p signal is a spin–orbit doublet and each chemical state consists of two peaks. The S 2p (XPS) can be fitted with two components at ~169.2 eV and ~170.5 eV, corresponding to a metal sulfate, here attributed to Li_2SO_4.[45] The HAXPES did not show the S 2p response but the signal from S 1s was detected. Two components at ~2477.9 eV and ~2480.0 eV can be used to fit S 1s spectra. However, since 1s core levels are singlet states, the two peaks in the S 1s peak suggest more than one chemical state, which may be related to sulfate in a different environment to surface Li_2SO_4 (*i.e.* bulk incorporation).

The recorded O 1s spectra from XPS and HAXPES are shown in Fig. 3c and d. The O 1s spectra (XPS) are fitted to two oxygen contributions at ~528.9 eV and ~531.8 eV, and the O 1s spectra (HAXPES) are fitted to three components at ~528.4 eV, ~531.4 eV and ~533.9 eV. The components at ~528 eV and ~531 eV are assigned to metal–oxygen bonds and carbonate groups, respectively.[46,47] The O 1s contribution above ~533 eV can be assigned to either water or sulfate bonds (both are located in this region).[48] Previous studies of sulfate incorporation into perovskite oxides have indicated associated oxygen vacancies are introduced.[33] The refinement of the structure for S-LRNO, however, reveals only a very small amount of oxygen vacancies in this case. Computational modelling (below) also suggests that generating oxygen vacancies within the layered structure is a high-energy, *i.e.*, unfavorable process. Hence, given that the amount of oxygen vacancies appears to be very low, their presence is difficult to detect by either XPS or HAXPES.

The chemical stability in ambient atmosphere of polyanion modified LNO was examined by exposing both undoped and

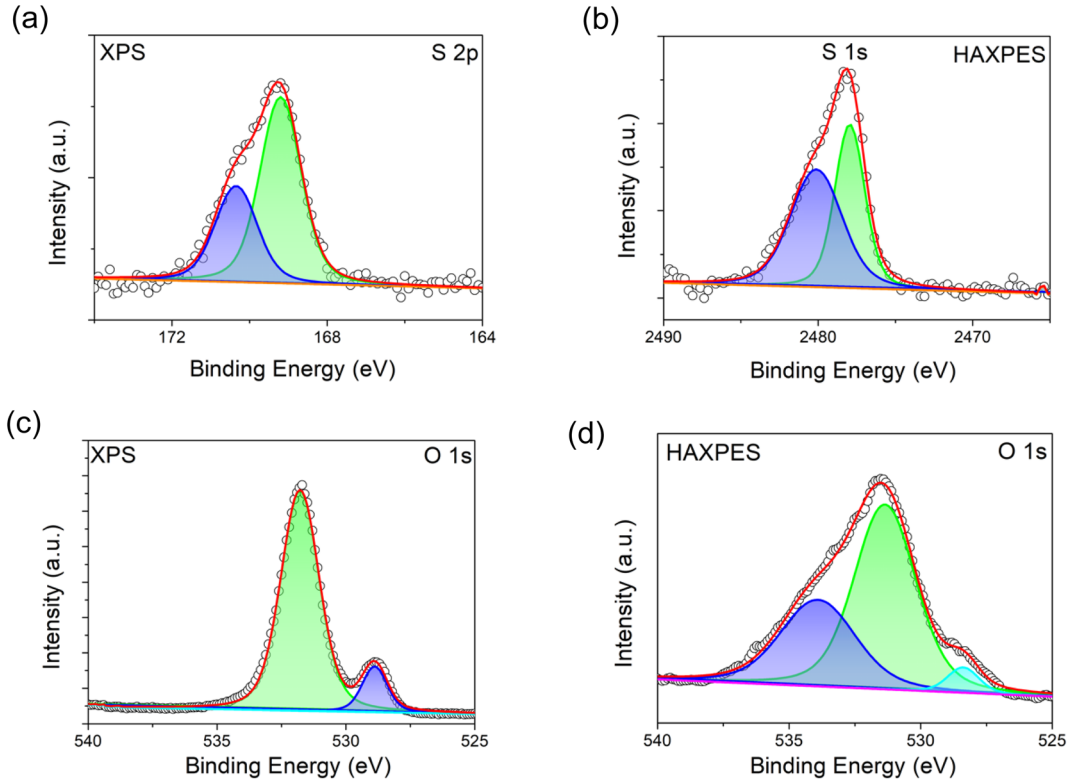

Fig. 3 XPS and HAXPES spectra of S-LRNO (solid state route). (a) XPS spectra of S 2p, (b) HAXPES spectra of S 1s, (c) XPS spectra of O 1s, and (d) HAXPES spectra of O 1s.

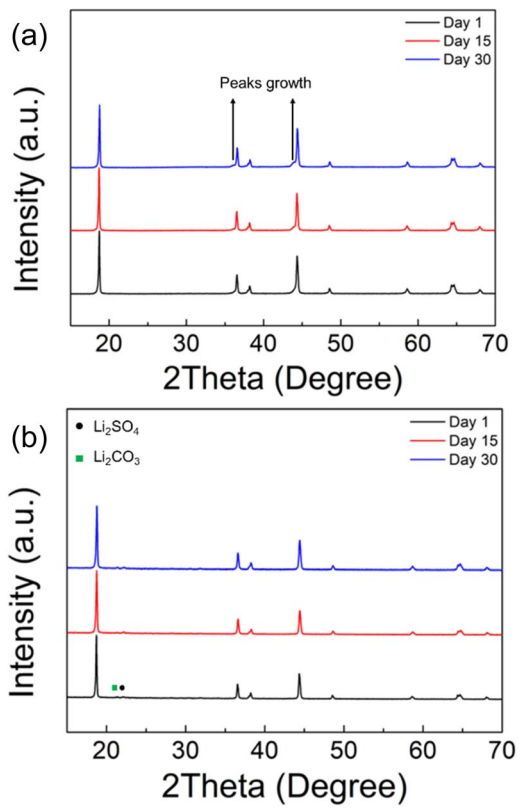

Fig. 4 XRD patterns of (a) $LiNiO_2$ and (b) $Li_{1.1}Ni_{0.85}S_{0.05}O_{2-\delta}$ (solid state route) after the exposure in air after 1, 15 and 30 days.

sulfate doped samples to air. The XRD results, as shown in Fig. 4a, shows a clear degradation in the undoped LNO sample with the detection of additional peaks at ~36 and ~44° after exposing to air for 2 weeks (zoomed-in region is shown in Fig. S2†). In contrast, sulfate modified LRNO showed no change under the same conditions (Fig. 4b), illustrating the improved stability in ambient atmosphere of this phase.

2.1.2 Atomic-scale insights from *ab initio* simulations. The defect chemistry of incorporation of S and excess Li into $LiNiO_2$ was further investigated by DFT simulations. To form Li-rich $LiNiO_2$, the excess Li is accommodated on the Ni site. Within the disproportionated structure of LNO,[49] the Li_{Ni} defect carries minimal structural distortions *versus* a high-spin Ni (octahedral volume 11.2 Å^3 *vs.* 10.9 Å^3) and induces a rearrangement of Ni spins around itself that is consistent with having one extra electron relative to a high-spin (formally "2+") Ni. This is in contrast with the common expectation of a double negative effective charge relative to a spin-half (formally "3+") nickel. A single negative charge on an excess Li on Ni (Li_{Ni}) relative to the lattice is consistent regardless of which site (high-spin, half-spin, or zero-spin) is substituted with Li to initialize the calculation in the spin-disproportionated structure. To maintain charge neutrality upon the inclusion of a Li_{Ni} defect, the compensating hole is accommodated as a hole polaron.[49]

At the conditions of synthesis (700 °C, 1 atm O_2) where layered LNO is in equilibrium with disordered rocksalt from which it is synthesized, the lowest-energy incorporation of

Table 4 Computed incorporation energies for select intrinsic defects in spin-disproportionated $LiNiO_2$ at synthesis conditions (700 °C, 1 atm O_2)

Defect	Incorporation energy (eV)	Compensation
Li_{Ni}	0.30	h_{Ni}
V_O	1.40	e_{Ni}
Ni_{Li}[49]	−0.12	e_{Ni}

dilute Li_{Ni} defects into the disproportionated structure is 0.30 eV (Table 4), which decreases with the supplied Li excess (increase in μ_{Li}).[42,50] The logical limit of such excess Li incorporation is Li_2NiO_3, where Li_{Ni} defects fully substitute one of three Ni sub-lattices, and all remaining Ni atoms have zero spin and are formally in a "4+" charge state. However, experimental attempts have only approached this limit with substantial Ni disorder and reduction;[26] layered Li_2NiO_3 has to our knowledge not been synthesized.

Turning to sulfate doping, the predicted lowest-energy site for the bulk incorporation of dilute S is S_{Ni} at 2.92 eV during synthesis (Table 5). The dopant S_{Ni} is surrounded and compensated by additional high-spin nickels, which approximate Ni^{2+}. Such compensation additionally relieves the mechanical stress created by extremely short S–O bonds (≈1.69 Å) of the S_{Ni} by surrounding it with enlarged Ni octahedra. We find it further instructive to compare the energetics of incorporation of sulfur with other common high-valence dopants such as W and Mo, which are known to phase-separate at interfaces and grain boundaries.[31,32] The incorporation energies for Mo_{Ni} and W_{Ni} are both under 1 eV, and the dopant–oxygen bond lengths are much closer to those of the parent nickel octahedra at 1.93 Å.

The association of S_{Ni} with oxygen vacancies (formation energy 1.40 eV on their own) is not favorable: the loss of coordination by the surrounding nickel offsets the favorability of approaching tetrahedral S, with an association energy of 0.85 eV (Table 6). This contrasts with polyanion doping of perovskites, where each oxygen anion is two-coordinate, and fewer metal–oxygen bonds are broken to accommodate the sulphur. The association of excess Li_{Ni} with S_{Ni} is only favorable by 20 meV (Table 6); such an effect does not translate to finite temperatures when the octahedra are dynamically disordered. Surface

Table 6 Computed association energies for defect complexes in spin-disproportionated $LiNiO_2$ at synthesis conditions (700 °C, 1 atm O_2). Negative is favorable, for consistency with Tables 4 and 5

Complex	Association energy (eV)
Li–Ni exchange	−0.05
S_{Ni} + Li_{Ni}	−0.02
S_{Ni} + Ni_{Li}	0.20
S_{Ni} + Li–Ni exchange	0.23
S_{Ni} + V_O	0.85

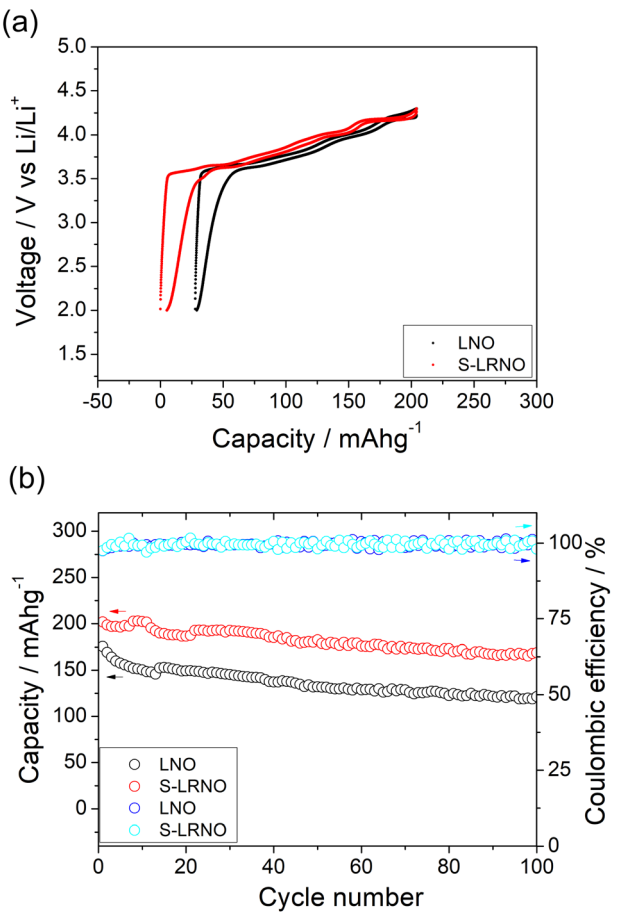

Fig. 5 (a) Initial charge–discharge curves of LNO and S-LRNO synthesised by the solid state method between 2 and 4.3 V at 25 mA g^{-1} (after the formation cycle). (b) The cycling performance of LNO and S-LRNO at 25 mA g^{-1}.

Table 5 Computed incorporation energies for select high-valence dopants in spin-disproportionated $LiNiO_2$ at synthesis conditions (700 °C, 1 atm O_2). Bond lengths are cited for dopant-oxygen bonds

Dopant	Incorporation energy (eV)	Chemical potential (eV)	Reference phase	Bond length (Å)
Mo_{Ni}	0.84	−6.29	Li_4MoO_5 (ref. 31)	1.93
W_{Ni}	0.91	−7.16	Li_4WO_5	1.93
S_{Ni}	2.92	−4.52	Li_2SO_4	1.69
$S_{Ni,(104)}$	6.93	−4.52	Li_2SO_4	1.59
$S_{Ni,(012)}$	4.57	−4.52	Li_2SO_4	1.57
$S_{Ni,(100)}$	4.56	−4.52	Li_2SO_4	1.59
$S_{Ni,(110)}$	4.96	−4.52	Li_2SO_4	1.57

incorporation at Ni sites has similarly unfavorable energetics (Table 5), although the figures are approximate due to the multitude of possibilities for compensation *via* polarons, O, and Li.

However, since Li_2SO_4 forms a eutectic with Li_2CO_3,[51] its addition can facilitate lithiation and crystallisation during the solid state synthesis of LNO at the experimental temperatures used here, which are below the melting point of Li_2CO_3. This positive effect is demonstrated by a small decrease in the full width at half maximum of XRD peaks in the sulfate modified sample prepared using the solid state route, as shown in Fig. S3.†

2.2 Electrochemical performance

2.2.1 Solid state method. The electrochemical properties of solid state reaction prepared $Li_{1.1}Ni_{0.85}S_{0.05}O_{2-\delta}$ (S-LRNO) and $LiNiO_2$ (LNO) were evaluated in the voltage range of 2.0–4.3 V. Fig. 5a shows the initial galvanostatic charge/discharge curves (after the formation cycle) as a function of capacity at 25 mA g^{-1} current density (charge rate ≈ C/10). The initial discharge capacities of S-LRNO increased to 203 mA h g^{-1} compared to 176 mA h g^{-1} for LNO. The formation cycle (Fig. S4 and S5†) at 25 mA g^{-1} indicates 11.5% and 7.8% capacity loss for LNO and S-LRNO respectively. The H2–H3 two-phase plateau is more prevalent in the S-LRNO sample compared to that of LNO. S-LRNO showed a higher voltage on both charging and discharging processes, leading to a higher energy density than that of LNO. Slightly reduced hysteresis and improved lower-voltage plateau were also observed for S-LRNO, demonstrating the benefits of sulfate modification. The cycling performance of selected cells was further evaluated at 25 mA g^{-1} for 100 cycles (Fig. 5b). After 100 cycles, the discharge capacities of $Li_{1.1}Ni_{0.85}S_{0.05}O_{2-x}$ were ~170 mA h g^{-1} compared to 130 mA h g^{-1} for LNO, illustrating the improved capacity retention (83.7% for S-LRNO and 73.8% for LNO) for the sulfate modified system.

To confirm the importance of sulfate incorporation in addition to surface coating, a separate experiment to introduce Li_2SO_4 as a coating was examined. Here the $Li_{1.1}Ni_{0.85}O_2$ was ball milled (500 rpm/1 h) with 5% Li_2SO_4 which is the equivalent sulfate content in the structure (sample named as coated-LRNO), and reheated at 700 °C/12 h in O_2. As shown in Fig. 6a, the XRD pattern of ball milled $Li_{1.1}Ni_{0.85}O_2$ (with Li_2SO_4) showed a layered phase with Li_2SO_4 impurity and a few unknown peaks. The electrochemical performance of

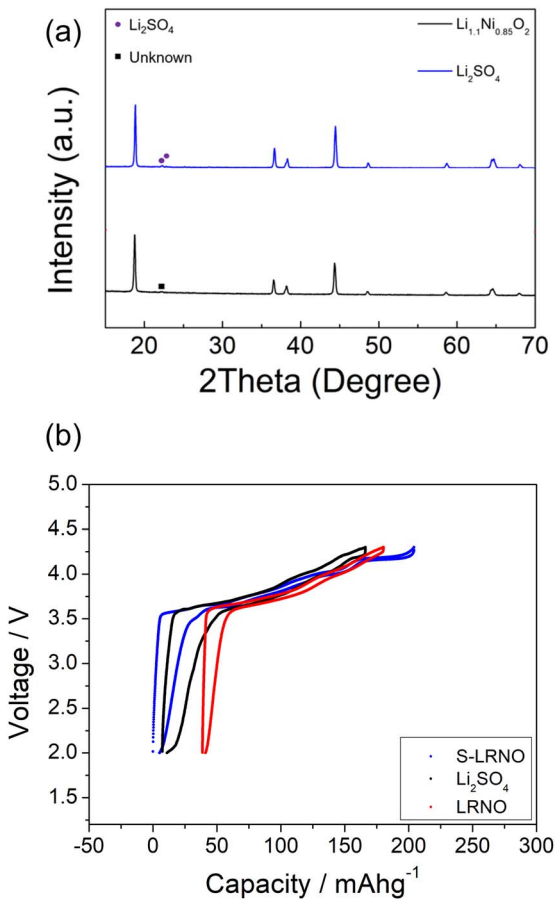

Fig. 6 (a) XRD patterns of $Li_{1.1}Ni_{0.85}O_{2-x}$, and Li_2SO_4 ball milled $Li_{1.1}Ni_{0.85}O_{2-x}$. (b) Charge–discharge curves of solid state route synthesised LRNO, S-LRNO and LRNO with 5%Li_2SO_4 between 2 and 4.3 V at 25 mA g^{-1} (after the formation cycle).

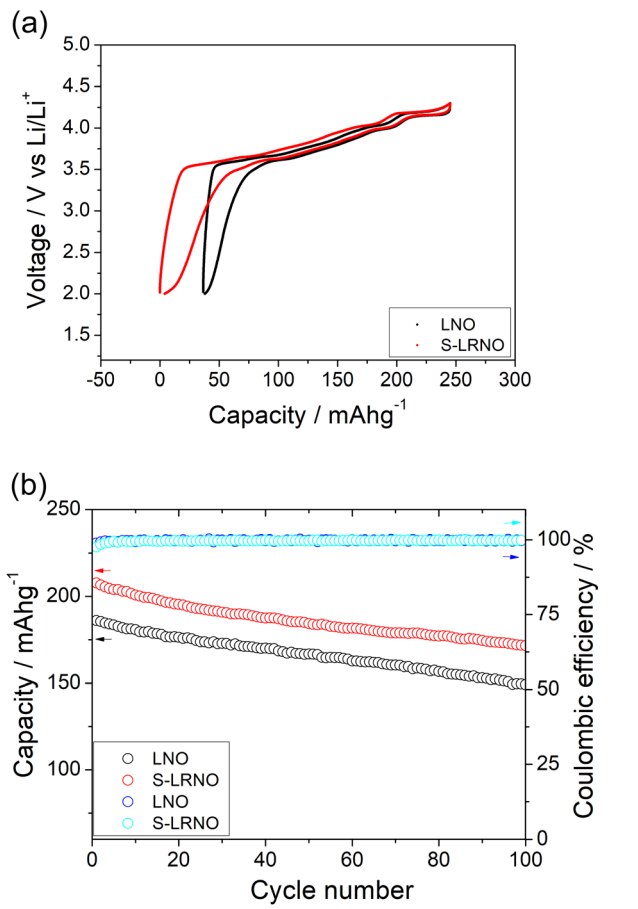

Fig. 7 (a) Initial charge–discharge curves LNO and S-LRNO synthesised by the co-precipitation route between 2 and 4.3 V at 25 mA g^{-1} (after the formation cycle). (b) The cycling performance of LNO and S-LRNO at 100 mA g^{-1}.

$Li_{1.1}Ni_{0.85}O_2$ (LRNO) and the 5% Li_2SO_4 coated $Li_{1.1}Ni_{0.85}O_2$ (coated-LRNO) was examined using the same conditions to that of S-LRNO. As shown in Fig. 6b, both LRNO and coated-LRNO showed poorer performance compared to that of S-LRNO, indicating the sulfate incorporation assisted with the formation of the lithium-excess phase. In addition, while the discharge capacities of coated-LRNO improved a little compared to LRNO, the values are much lower than S-LRNO (Fig. 6b and S6†), which further supports the successful sulfate incorporation in the original sample. The improved electrochemical performance could result from both the limited sulfate dopant in the structure and the Li_2SO_4 passivating layers which is spontaneously formed beyond the solid solution limitation, in addition to the Li_2SO_4–Li_2CO_3 eutectic effects facilitating high lithiation and crystallization in the solid state synthesis (as mentioned in the modelling section).

2.2.2 Co-precipitation method. Following promising results from solid state synthesis, a co-precipitation route, which is the preferred industrial route, was further investigated to enhance the performance, as illustrated previously for undoped stoichiometric $LiNiO_2$.[20] The LNO prepared using the co-precipitation route exhibited a (003/104) ratio of 1.679 which is higher than that of the sample prepared using the solid state route, demonstrating a more ordered structure. For both LNO and S-LRNO samples, the use of a co-precipitation route was shown to improve the electrochemical performance under cycling between 2.0 V and 4.3 V at 25 mA g^{-1} (Fig. 7a). The discharge capacity of S-LRNO increases to ~245 mA h g^{-1} compared to ~223 mA h g^{-1} for LNO, with the former value representing an excellent initial capacity significantly exceeding traditional Mn and Co doped systems, $Li(Ni,Mn,Co)O_2$. A higher average voltage with similar voltage hysteresis was seen for S-LRNO during intercalation above 3.5 V, and a slightly increased hysteresis was seen at lower voltage for S-LRNO. The cycling performance of selected cells was also conducted at 100 mA g^{-1} (charge rate ≈ C/2, initial discharge capacity ~ 205 mA h g^{-1}), which was chosen to represent a commercially relevant rate. The results showed that the discharge capacity of S-LRNO after 100 cycles remained ~171 mA h g^{-1} (Fig. 7b). Although a first cycle loss of ~12.3% in S-LRNO at 100 mA g^{-1} was observed (Fig. S7 and S8†), 83.4% capacity retention was achieved which is higher than 80.5% for LNO over 100 cycles.

Rate capabilities of co-precipitated LNO and S-LRNO were then tested in the voltage range of 2.0–4.3 V at current densities of 25, 50, 100, 200, 400 and 25 mA g^{-1} for 5 cycles (Fig. 8a). The discharge capacities of co-precipitated S-LRNO and LNO reached 230 and 209 mA h g^{-1} at 25 mA g^{-1}, 207 and 176 mA h g^{-1} at 50 mA g^{-1}, 192 and 165 mA h g^{-1} at 100 mA g^{-1}, 176 and 145 mA h g^{-1} at 200 mA g^{-1}, 161 and 117 mA h g^{-1} at 400 mA g^{-1} respectively. The S-LRNO sample exhibits higher

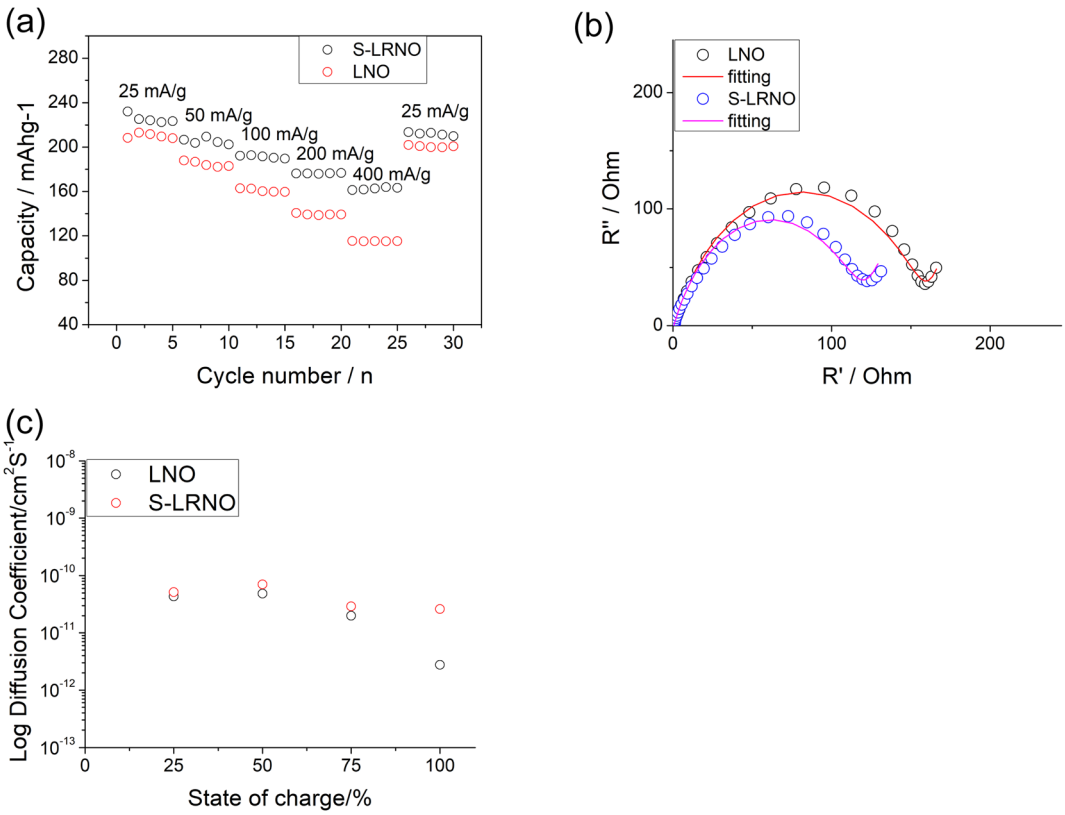

Fig. 8 (a) The cycling performance of LNO and S-LRNO prepared using co-precipitation route at different rates. (b) EIS of LNO and S-LRNO prepared using co-precipitation route at the 1st cycle. (c) GITT of LNO and S-LRNO prepared using co-precipitation route on charging at the initial cycle (after formation cycles).

Table 7 EIS fitting parameters for LNO and S-LRNO

Parameter	LNO	S-LRNO
R_1 (Ω)	1.5	1.4
R_{CT} (Ω)	160	119

discharge capacities than those of the pristine LNO at all cycling rates, illustrating the improved rate capability of the sulfate modified sample.

Electrochemical impedance spectroscopy analysis for both samples are shown in Fig. 8b. The smaller semicircle was seen in S-LRNO than that of LNO, indicating a smaller internal resistance. By fitting the Nyquist plots with the equivalent circuit, the S-LRNO shows a charge transfer resistance of 119 Ω which is lower than 160 Ω in LNO (Table 7). To investigate the influence of sulfate modification on the kinetic behavior of Li^+, GITT (galvanostatic intermittent titration technique) was carried out to determine the apparent diffusion capability of Li^+ in the initial cycle (after formation cycles). The D_{Li} calculated from the GITT curve as a function of the state of charge during charging are shown in Fig. 8c, where the measured solid-state diffusion coefficient is mainly in the range of 10^{-12} to 10^{-11}. The sulfate doped sample exhibits an increased D_{Li} value compared to LNO, indicating faster kinetics for Li ion in the doped sample. Although the SEM analyses of LNO and S-LRNO prepared using the co-precipitation route revealed comparable morphology of particles (Fig. 9), the observed enhancements in rate capability and lithium transport kinetics in S-LRNO could be attributed to the excess lithium ions in the structure; this feature helps to promote the formation of face-sharing or edge-sharing lithium octahedra, leading to reduced lithium ion hopping distance and lower activation energy.

The structural transitions during the cycling of doped and undoped LRNO prepared using co-precipitation routes was evaluated using dQ/dV curves, as shown in Fig. 10; H1–M, M–H2, and H2–H3 phase transitions were observed for both materials, which is consistent with literature.[11] In contrast to the quickly decaying H2–H3 phase transition in undoped LNO, this transition has been preserved after long-term cycling for sulfate doped samples, as shown in Fig. 9d. This result suggests that structural changes during the cycling for the sulfate modified phase are more reversible, which most likely accounts for the improved long-term capacity. In this respect, it has been reported that high valence dopants, such as Mo^{6+} and W^{6+}, in $LiNiO_2$, could facilitate the merging of the Li-rich and Li-poor phases into a single phase during the H2–H3 phase transition, resulting in better structural stability.[28,31] Other studies have shown that high valence dopants help to suppress primary particle growth during synthesis and impart mechanical toughness to counteract the high internal strain.[32,52] The introduction of excess Zr^{4+}

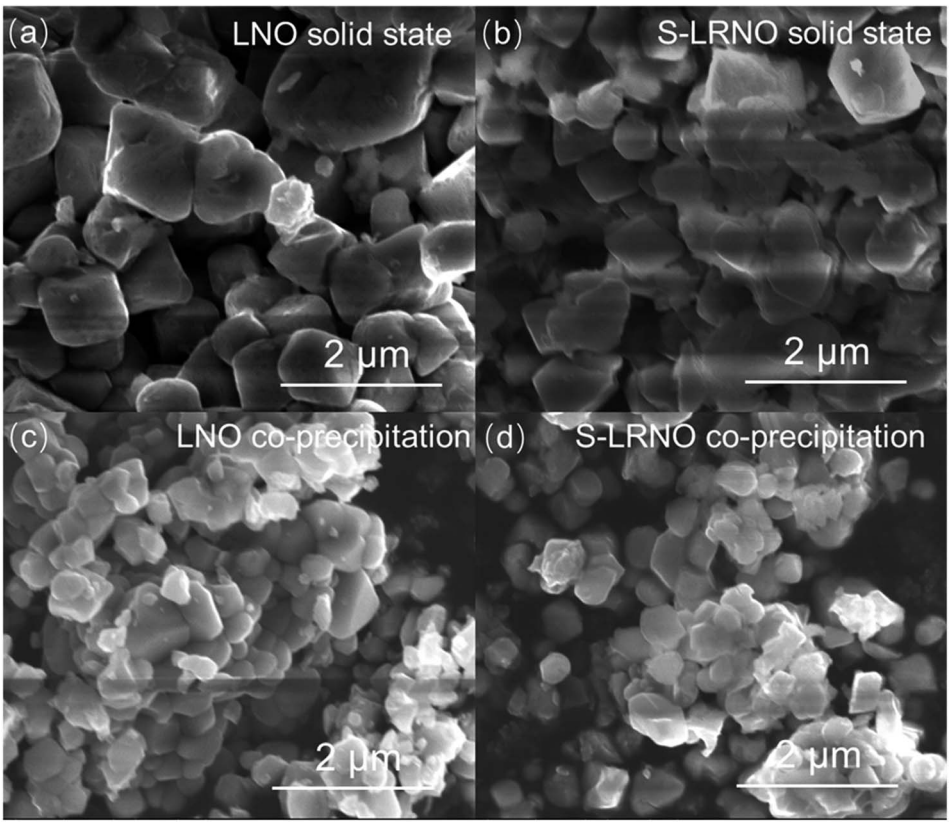

Fig. 9 SEM images of samples at 50 000× magnification (a) LNO prepared by solid state route (b) S-LRNO prepared by solid state route (c) LNO prepared by co-precipitation route (d) S-LRNO prepared by co-precipitation route.

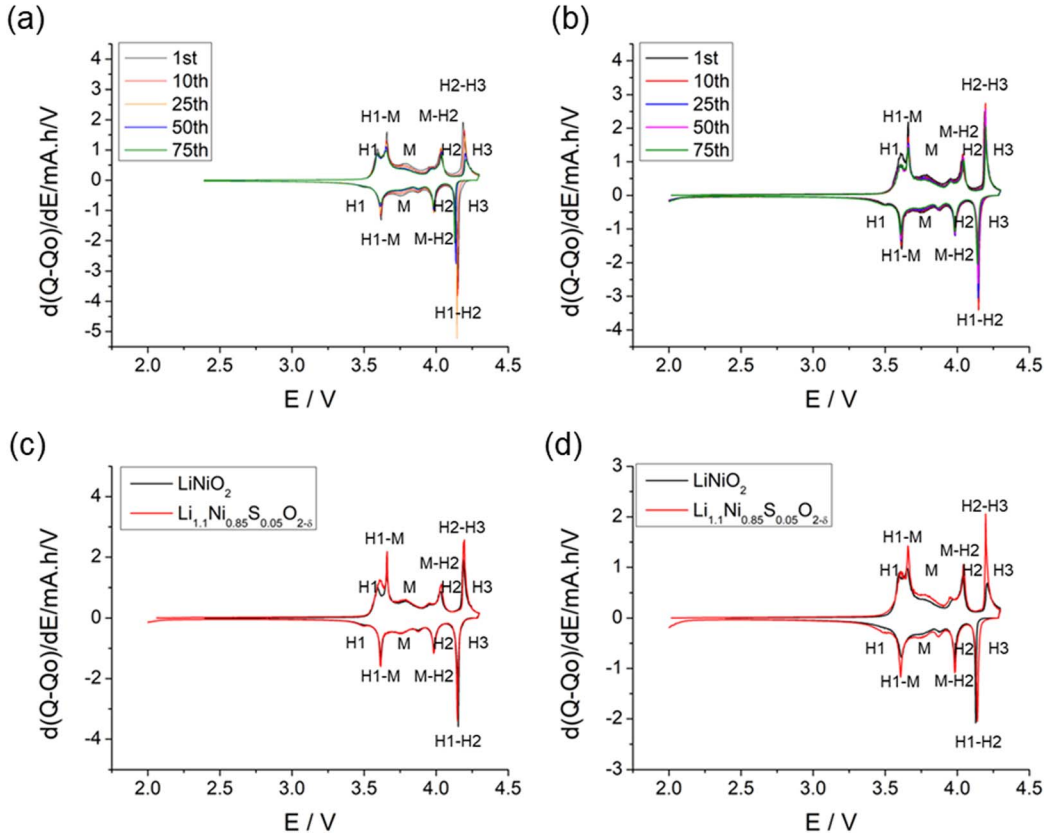

Fig. 10 dQ/dV curves of (a) $LiNiO_2$ and (b) $Li_{1.1}Ni_{0.85}S_{0.05}O_{2-x}$ prepared through co-precipitation route; (c) comparison of $LiNiO_2$ and $Li_{1.1}Ni_{0.85}S_{0.05}O_{2-x}$ at 1st cycle. (d) Comparison of $LiNiO_2$ and $Li_{1.1}Ni_{0.85}S_{0.05}O_{2-x}$ at 75th cycle showing the clear preservation of H2–H3 transition in the latter.

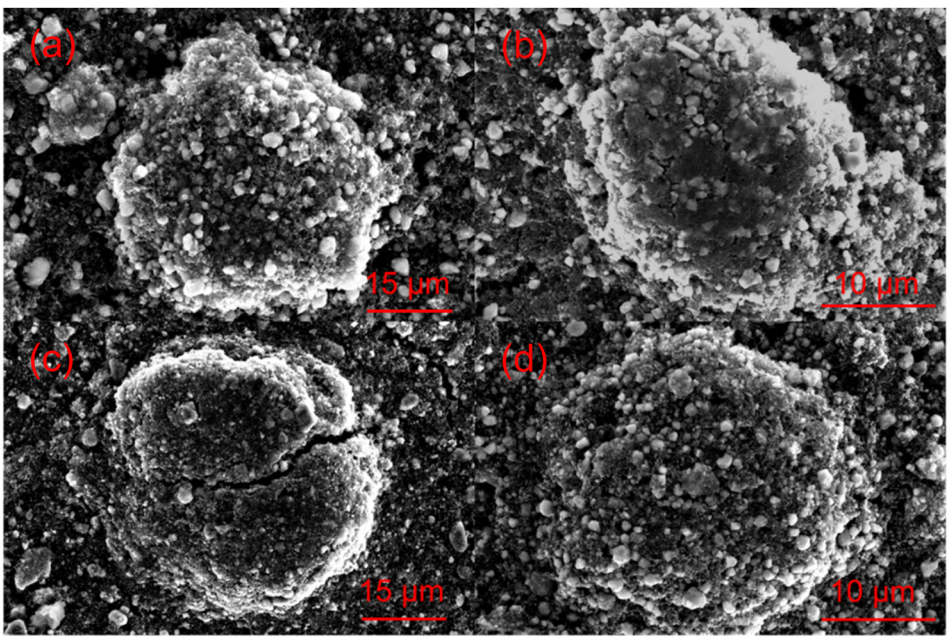

Fig. 11 SEM images of (a) pristine $LiNiO_2$; (b) pristine $Li_{1.1}Ni_{0.85}S_{0.05}O_{2-x}$ (c) $LiNiO_2$ after 200 cycles. (d) $Li_{1.1}Ni_{0.85}S_{0.05}O_{2-x}$ after 200 cycles.

into the $LiNiO_2$ cathode was shown to result in simultaneous doping and coating with Li_2ZrO_3, enhancing the phase transition and thermal stability,[23] similar to what we observe for sulfate doping (small incorporation with Li_2SO_4 coating). The SEM images of S-LRNO and LNO before and after 200 cycles are shown in Fig. 11, where cracking was observed for LNO whereas S-LRNO showed better particle preservation, illustrating further the benefits of sulfate modification.

3. Conclusions

Polyanion (sulfate) modified $LiNiO_2$ and Li-rich $LiNiO_2$ were synthesised through solid state and co-precipitation methods. Although the solid solution of sulfate doping appears to be limited in line with modelling results, a self-passivation Li_2SO_4 layer formed beyond the solid solution, which contributed to the improvement in air stability and to the electrochemical performance of sulfate modified Li-rich $LiNiO_2$ (S-LRNO).

Such improved electrochemical performance as well as better capacity retention for S-LRNO was observed for samples prepared using both solid state and co-precipitation methods. The initial 245 mA h g^{-1} discharge capacity (at 25 mA g^{-1}) for co-precipitation synthesised S-LRNO represents a significant improvement to conventional Mn and Co co-doped NMC systems. High capacities were also observed at higher rates (205 mA h g^{-1} initial discharged capacity at 100 mA g^{-1}), with improved capacity retention compared to the unmodified system and attributed to the improved preservation of the H2–H3 transition. Overall, this work highlights that as an alternative design strategy, polyanion modification can effectively improve the electrochemical properties of lithium nickel oxide cathode materials, which has the potential to be easily applied to other cathode systems.

4. Experimental

4.1 Synthesis

For the solid state synthesis method, Li_2CO_3 (99.9%, Alfa Aesar), $Ni(NO_3)_2 \cdot 6H_2O$ (%, Sigma-Aldrich), $(NH_4)_2SO_4 \cdot H_2O$ (99%, Sigma-Aldrich), $(NH_4)H_2PO_4$ (99%, Sigma-Aldrich) and SiO_2 (99%, Sigma-Aldrich) were used as reagents. $Li_{1+z}Ni_{1-z-x}M_xO_{2-y}$ (M = S, P, Si) samples from intimately ground stoichiometric amounts of starting reagents were heated initially to 650 °C for 12 hours at a rate of 2.5 °C min^{-1} to fully decompose starting reagents. A 2.5% excess Li_2CO_3 was added to the mixture to compensate for Li loss during the synthesis. The mixture was milled (ZrO_2 containers and balls) with hexane solvent for 30 minutes using a Pulverisette 5 planetary ball mill to yield fine powders. The powders were pressed into pellets and reheated one or multiple times at 700–725 °C for 12 hours in dry O_2 with a rate of 5 °C min^{-1} to obtain the final product, which is stored in an Ar-filled glove box.

For co-precipitation method, $Ni(OH)_2$ precursor were synthesised by precipitation from an aqueous solution of $Ni(NO_3)_2 \cdot 6H_2O$ and NaOH. Then $(NH_4)_2SO_4 \cdot H_2O$ (99%, Sigma-Aldrich), $Ni(OH)_2$ (as prepared) and $LiOH \cdot H_2O$ (99%, Sigma-Aldrich) were mixed with 5–10% excess $LiOH \cdot H_2O$ by ball milling in a zirconia pot at 500 rpm for 1 hour. The mixture was heated to 350 °C for 12 hours at 2.5 °C min^{-1} and followed by heating to 700 °C for 12 hours at 5 °C min^{-1} in O_2 to obtain the final product. The sample was allowed to cool down to room temperature and stored in an Ar-filled glove box.

4.2 X-ray diffraction

A Bruker D8 X-ray diffractometer (XRD) with CuKα radiation and linear position sensitive detector was used to collect X-ray diffraction data. Patterns were recorded over the 2θ range 15° to 80° with a 0.02° step size. Structural refinement was carried out using the XRD data with the GSAS suite of Rietveld refinement software.[53]

4.3 Neutron diffraction

The neutron diffraction experiment was performed on the POWGEN instrument at the Spallation Neutron Source (SNS), Oak Ridge National Laboratory. Approximately 1 g of powder was loaded into a PAC vanadium can with 6 mm diameter. The sample cans were loaded into POWGEN sample changer (PAC) and the diffraction data was collected at 293 K for around 2 hour, followed by the standard data reduction routine. The center wavelength was 0.8 Å, covering a d spacing range of 6.2 Å > d > 0.1 Å.

4.4 Electrochemical testing

The active materials and carbon black (TimCal, C65) were dried at 110 °C for 24 h in a vacuum oven before use. The slurry was prepared by mixing 80% active materials, 10% carbon black and 10% polyvinylidene fluoride (PVDF, PI-KEM) in *N*-methyl-2-pyrrolidine (NMP, Sigma) using a Thinky mixer, before coating onto an aluminum foil in a dry room. The cathode was dried at 120 °C for 24 h in the vacuum oven and punched into 14.8 mm disks. The electrode disks were weighed and the mass loading of active materials on cathodes was 3–4 mg cm^{-2}. Li metal (Aldrich) was used as anode, which was rolled and punched into 15 mm disks. The composition of the electrolyte (R&D 281, Soulbrain) was 1.0 M $LiPF_6$ in EC : EMC (ethylene carbonate/methyl carbonate, 3/7 V/V) with 1 wt% VC (vinylene carbonate) as an electrolyte additive. Microporous trilayer membrane (PP/PE/PP) (H1609, Celgard) was used as the separator.

The half cells using the components above were assembled with CR2032 coin cells in an argon-filled glove box and all electrochemical measurements were conducted on the BCS805 cell tester (Bio-logic). Galvanostatic charge/discharge with potential limitation (GVPL) measurement was conducted at constant current density of 25 mA g^{-1}, 50 mA g^{-1} or 100 mA g^{-1} in the voltage range between 2 and 4.3 V *vs.* Li/Li^+. Electrochemical impedance spectroscopy (EIS) measurement was performed in half-cell using an amplitude of 5 mV in the frequency range from 10^{-2} to 10^5 Hz. For the data analysis, EC-Lab software was used for the equivalent circuit models fitting.

For galvanostatic intermittent titration technique (GITT) measurement, the cells were charged and discharged at 25 mA g^{-1} with a rest (3 h) to achieve full equilibrium voltage. Fundamental ideas calculating diffusion coefficients from GITT technique have originated from the research work by Weppner

and Huggins.[54] Here we adopted the transformed sand equation to calculate the diffusion of Li^+ in the active particle materials from the following eqn (1).

$$D_{Li^+} = \frac{4}{\pi}\left(\frac{iV_m}{nFS}\right)^2\left(\frac{dE/d\delta}{dE/dt^{0.5}}\right)^2 \quad (1)$$

Herein, i denotes the current passing through the electrode with the unit of amps (A); V_m is the molar volume of active materials ($cm^3\ mol^{-1}$); n stands for the transferred electrons in the 'reaction' ($n = 1$); F and S are Faraday constant ($C\ mol^{-1}$) and active surface area between electrode and electrolyte (m^2); the gradient $dE/d\delta$ is the slope of the coulometric titration curve, which is found by plotting the steady state voltages $E(V)$ measured after each titration step. The gradient $dE/dt^{0.5}$ means the slope of the linearized plot of the potential $E(V)$ during the current pulse of duration.

The rate tests for LNO and S-LRNO prepared using co-precipitation routes were performed in hall cells using different current densities at 25, 50, 100, 200, 400 mA g^{-1} within the voltage window of 2 to 4.3 V *vs.* Li/Li^+.

4.5 X-ray absorption spectroscopy (XAS), X-ray photoelectron spectroscopy (XPS) and hard X-ray photoelectron spectroscopy (HAXPES)

Hard X-ray absorption spectroscopy (XAS) data at the Ni K-edge of NiO, $LiNiO_2$ and S-LNRO were measured at the beamline, Diamond Light Source. X-ray photoelectron spectroscopy (XPS) and hard X-ray photoelectron spectroscopy (HAXPES) were measured on one instrument (HAXPES-Lab, Scienta Omicron GmbH). Hard X-ray photoelectron spectroscopy (HAXPES) was performed using monochromated Ga Kα metal jet X-ray radiation (9252 eV, 3.57 mA emission at 250 W, micro-focussed to 50 μm) and an EW-4000 high voltage electron energy analyser (HAXPES-Lab, Scienta Omicron GmbH); the instrument has a base vacuum pressure of 5×10^{-10} mbar.[55,56] The entrance slit width used was 1.5 mm, and the pass energies used for survey and core level spectra were 500 and 100 eV respectively, with total energy resolutions of 2.0 and 0.6 eV respectively.[55] The HAXPES instrument also has a monochromated Al Kα X-ray source (1486 eV, 20 mA emission at 300 W) for surface sensitive XPS at the same sample position. Charge neutralisation for insulating samples is achieved using a low energy electron flood source as required (FS40A, PreVac). Binding energy scale calibration was performed using Au 4f7/2 at 84 eV of a clean gold reference sample, else C 1s at 285 eV BE if the flood source is used. Analysis and curve fitting was performed using Voigt-approximation peaks using CasaXPS.[57] Core level relative sensitivity factors for HAXPES quantification were calculated according to references.[56,58]

4.6 Computational methods

All calculations were performed within the density functional theory (DFT) framework using the Vienna *ab initio* Simulation Package (VASP).[59–62] Following our work on undoped $LiNiO_2$,[49] the calculations were performed using the meta-generalized gradient approximation r^{2}SCAN functional with the revised Vydrov–van Voorhis (rVV10) non-local dispersion correction.[63] All calculations were after convergence tests performed with a plane-wave cutoff of 700 eV, projector augmented wave (PAW) pseudopotentials to describe the core electrons,[64] and k-point spacing of 0.25 $Å^{-1}$. The convergence criteria were set to $\leq 10^{-5}$ eV for energies and $\leq 10^{-2}$ eV $Å^{-1}$ for forces. Unless otherwise stated, the relaxation calculations were started from the spin-disproportionated hexagonal structure;[49] zigzag $P2_1/c$ structure was also computed.

The chemical potentials of the elements (μ_O, μ_{Li}, μ_{Ni}, μ_S) have a direct impact on the calculated defect formation energies. All chemical potentials were chosen to represent the conditions of the material synthesis, where the partial pressure of oxygen and temperature are set by the phase equilibrium between the forming LNO phase and a disordered rocksalt $Li_xNi_{1+x}O_2$ ($x < 1$) phase at 700 °C and 1 atm O_2, which yields $\mu_{Li} = -3.00$ eV and $\mu_{Ni} = -1.35$ eV.[49] The chemical potentials of extrinsic dopants were set by a phase equilibrium with another phase, such as Li_2SO_4 for S, at the same temperature and oxygen pressure ($\mu_S = -4.52$ eV, Table 5). The magnetic moments of the Ni ions were used as simple proxies for their charge states. Such DFT based methods have been applied to a wide range of Li-ion cathode materials.[65–69]

Author contributions

Bo Dong: conceptualization, data curation, formal analysis, investigation, methodology, visualization, writing – original draft, writing – review & editing. Andrey Poletayev: data curation, formal analysis, investigation, methodology, visualization, writing – original draft, writing – review & editing. Jonathon P. Cottom: data curation, formal analysis, writing – original draft. Javier Castells-Gil: data curation, formal analysis, writing – original draft. Ben Spencer: data curation, formal analysis, writing – original draft. Cheng Li: data curation, formal analysis, writing – original draft. Pengcheng Zhu: data curation, formal analysis, writing – original draft. Yongxiu Chen: data curation, formal analysis, writing – original draft. Jaime-Marie Price: data curation, formal analysis. Laura L. Driscoll: data curation, formal analysis. Phoebe K. Allan: resources, supervision, writing – review & editing. Emma Kendrick: resources, supervision, writing – review & editing. M. Saiful Islam: conceptualization, funding acquisition, investigation, methodology, project administration, resources, supervision, writing – original draft, writing – review & editing. Peter R. Slater: conceptualization, funding acquisition, investigation, methodology, project administration, resources, supervision, writing – original draft, writing – review & editing.

Conflicts of interest

The authors declare no conflict of interest.

Acknowledgements

We would like to thank the Faraday Institution CATMAT (FIRG016, EP/S003053/1) and NEXTRODE (FIRG015) projects

for funding. We would like to thank the Diamond Light Source for the award of beam time as part of the Energy Materials Block Allocation Group SP14239. The XPS/HAXPES work was supported by the Henry Royce Institute, funded through EPSRC grants EP/R00661X/1, EP/P025021/1 and EP/P025498/1. We are also grateful to the HEC Materials Chemistry Consortium (EP/R029431) for the use of Archer2 high-performance computing (HPC) facilities, and for the Faraday Institution's Michael HPC resource. A portion of this research used resources at the Spallation Neutron Source, as appropriate, a DOE Office of Science User Facility operated by the Oak Ridge National Laboratory. J. C.-G. thanks the Generalitat Valenciana for his GVA APOSTD Fellowship (CIAPOS/2021/272). Raw experimental data can be found at **https://doi.org/10.25500/edata.bham.00001084**.

References

1 J.-M. Tarascon and M. Armand, *Nature*, 2001, **414**, 359–367.
2 P. G. Bruce, B. Scrosati and J. M. Tarascon, *Angew. Chem., Int. Ed.*, 2008, **47**, 2930–2946.
3 X. Zeng, M. Li, D. Abd El-Hady, W. Alshitari, A. S. Al-Bogami, J. Lu and K. Amine, *Adv. Energy Mater.*, 2019, **9**, 1900161.
4 F. Wu, J. Maier and Y. Yu, *Chem. Soc. Rev.*, 2020, **49**, 1569–1614.
5 J. Kim, H. Lee, H. Cha, M. Yoon, M. Park and J. Cho, *Adv. Energy Mater.*, 2018, **8**, 1702028.
6 T. Y. Li, X. Z. Yuan, L. Zhang, D. T. Song, K. Y. Shi and C. Bock, *Electrochem. Energy Rev.*, 2019, **3**, 43–80.
7 W. D. Li, E. M. Erickson and A. Manthiram, *Nat. Energy*, 2020, **5**, 26–34.
8 M. Bianchini, M. Roca-Ayats, P. Hartmann, T. Brezesinski and J. Janek, *Angew. Chem., Int. Ed.*, 2019, **58**, 10434–10458.
9 Y. Kim, W. M. Seong and A. Manthiram, *Energy Storage Mater.*, 2021, **34**, 250–259.
10 M. Guilmard, L. Croguennec, D. Denux and C. Delmas, *Chem. Mater.*, 2003, **15**, 4476–4483.
11 H. S. Liu, Z. R. Zhang, Z. L. Gong and Y. Yang, *Electrochem. Solid-State Lett.*, 2004, **7**, A190–A193.
12 W. Li, J. N. Reimers and J. R. Dahn, *Solid State Ionics*, 1993, **67**, 123–130.
13 C. Delmas, J. P. Pérès, A. Rougier, A. Demourgues, F. Weill, A. Chadwick, M. Broussely, F. Perton, Ph. Biensan and P. Willmann, *J. Power Sources*, 1997, **68**, 120–125.
14 R. Moshtev, P. Zlatilova, S. Vasilev, I. Bakalova and A. Kozawa, *J. Power Sources*, 1999, **81–82**, 434–441.
15 H. Y. Li, N. Zhang, J. Li and J. R. Dahn, *J. Electrochem. Soc.*, 2018, **165**, A2985–A2993.
16 L. Croguennec, C. Pouillerie, A. N. Mansour and C. Delmas, *J. Mater. Chem.*, 2001, **11**, 131–141.
17 M. Mock, M. Bianchini, F. Fauth, K. Albe and S. Sicolo, *J. Mater. Chem. A*, 2021, **9**, 14928–14940.
18 C. S. Yoon, D.-W. Jun, S.-T. Myung and Y.-K. Sun, *ACS Energy Lett.*, 2017, **2**, 1150–1155.
19 H. M. Qian, H. Q. a. Ren, Y. Zhang, X. F. He, W. B. Li, J. J. Wang, J. H. Hu, H. Yang, H. M. K. Sari, Y. Chen and X. F. Li, *Electrochem. Energy Rev.*, 2022, **5**, 1–32.
20 D. Weber, J. Lin, A. Pokle, K. Volz, J. Janek, T. Brezesinski and M. Bianchini, *J. Electrochem. Soc.*, 2022, **169**, 030540.
21 S. L. Dreyer, P. Kurzhals, S. B. Seiffert, P. Müller, A. Kondrakov, T. Brezesinski and J. Janek, *J. Electrochem. Soc.*, 2023, **170**, 060530.
22 J. L. Cheng, B. Ouyang and K. A. Persson, *ACS Energy Lett.*, 2023, **8**, 2401–2407.
23 C. S. Yoon, U.-H. Kim, G.-T. Park, S. J. Kim, K.-H. Kim, J. Kim and Y.-K. Sun, *ACS Energy Lett.*, 2018, **3**, 1634–1639.
24 L. Mu, R. Zhang, W. H. Kan, Y. Zhang, L. Li, C. Kuai, B. Zydlewski, M. M. Rahman, C.-J. Sun, S. Sainio, M. Avdeev, D. Nordlund, H. L. Xin and F. Lin, *Chem. Mater.*, 2019, **31**, 9769–9776.
25 M. Guilmard, *J. Power Sources*, 2003, **115**, 305–314.
26 Y. You, H. Celio, J. Li, A. Dolocan and A. Manthiram, *Angew. Chem., Int. Ed.*, 2018, **57**, 6480–6485.
27 Q. Xie, W. Li and A. Manthiram, *Chem. Mater.*, 2019, **31**, 938–946.
28 H.-H. Ryu, G.-T. Park, C. S. Yoon and Y.-K. Sun, *J. Mater. Chem. A*, 2019, **7**, 18580–18588.
29 D. Rathore, C. Geng, N. Zaker, I. Hamam, Y. L. Liu, P. H. Xiao, G. A. Botton, J. Dahn and C. Y. Yang, *J. Electrochem. Soc.*, 2021, **168**, 120514.
30 J.-M. Price, P. K. Allan and P. R. Slater, *Energy Adv.*, 2023, **2**, 864–876.
31 B. Li, G. Rousse, L. T. Zhang, M. Avdeev, M. Deschamps, A. M. Abakumov and J.-M. Tarascon, *Energy Environ. Sci.*, 2023, **16**, 1210–1222.
32 C. X. Geng, D. Rathore, D. Heino, N. Zhang, I. Hamam, N. Zaker, G. A. Botton, R. Omessi, N. Phattharasupakun, T. Bond, C. Y. Yang and J. R. Dahn, *Adv. Energy Mater.*, 2021, **12**, 2103067.
33 A. Orera and P. R. Slater, *Chem. Mater.*, 2010, **22**, 675–690.
34 C. A. Hancock, R. C. T. Slade, J. R. Varcoe and P. R. Slater, *J. Solid State Chem.*, 2011, **184**, 2972–2977.
35 C. A. Hancock and P. R. Slater, *Dalton Trans.*, 2011, **40**, 5599–5603.
36 J. M. Porras-Vazquez and P. R. Slater, *J. Power Sources*, 2012, **209**, 180–183.
37 J. M. Porras-Vazquez, T. Pike, C. A. Hancock, J. F. Marco, F. J. Berry and P. R. Slater, *J. Mater. Chem. A*, 2013, **1**, 11834–11841.
38 J. Deakin, I. Trussov, A. Gibbs, E. Kendrick and P. R. Slater, *Dalton Trans.*, 2018, **47**, 12901–12906.
39 L. D. Santos-Gómez, J. M. Porras-Vázquez, E. R. Losilla, D. Marrero-López and P. R. Slater, *J. Alloys Compd.*, 2020, **835**, 155437.
40 Y. Pan, X. Xu, Y. Zhong, L. Ge, Y. Chen, J. M. Veder, D. Guan, R. O'Hayre, M. Li, G. Wang, H. Wang, W. Zhou and Z. Shao, *Nat. Commun.*, 2020, **11**, 2002.
41 J. Deakin and P. Slater, *J. Solid State Chem.*, 2021, **294**, 121870.
42 M. Bianchini, A. Schiele, S. Schweidler, S. Sicolo, F. Fauth, E. Suard, S. Indris, A. Mazilkin, P. Nagel, S. Schuppler, M. Merz, P. Hartmann, T. Brezesinski and J. Janek, *Chem. Mater.*, 2020, **32**, 9211–9227.

43 C. Lee, Y. Yokoyama, Y. Kondo, Y. Miyahara, T. Abe and K. Miyazaki, *ACS Appl. Mater. Interfaces*, 2020, **12**, 56076–56085.
44 R. Fantin, T. Jousseaume, R. Ramos, G. Lefevre, A. Van Roekeghem, J.-P. Rueff and A. Benayad, *ACS Energy Lett.*, 2024, DOI: **10.1021/acsenergylett.4c00360**.
45 S. Contarini and J. W. Rabalais, *J. Electron Spectrosc. Relat. Phenom.*, 1985, **35**, 191–201.
46 G. P. López, D. G. Castner and B. D. Ratner, *Surf. Interface Anal.*, 1991, **17**, 267–272.
47 J. F. Marco, J. R. Gancedo, J. Ortiz and J. L. Gautier, *Appl. Surf. Sci.*, 2004, **227**, 175–186.
48 M. Wahlqvist and A. Shchukarev, *J. Electron Spectrosc. Relat. Phenom.*, 2007, **156–158**, 310–314.
49 A. D. Poletayev, J. P. Cottom, B. J. Morgan and M. S. Islam, *arXiv*, 2022, preprint, arXiv:2211.09047, DOI: **10.48550/arXiv.2211.09047**.
50 J. Cheng, L. Mu, C. Wang, Z. Yang, H. L. Xin, F. Lin and K. A. Persson, *J. Mater. Chem. A*, 2020, **8**, 23293–23303.
51 Y. Dessureault, J. Sangster and A. D. Pelton, *J. Electrochem. Soc.*, 1990, **137**, 2941–2950.
52 G.-T. Park, D. R. Yoon, U.-H. Kim, B. Namkoong, J. Lee, M. M. Wang, A. C. Lee, X. W. Gu, W. C. Chueh, C. S. Yoon and Y.-K. Sun, *Energy Environ. Sci.*, 2021, **14**, 6616–6626.
53 B. H. Toby, *J. Appl. Crystallogr.*, 2001, **34**, 210–213.
54 W. Weppner and R. A. Huggins, *J. Electrochem. Soc.*, 1977, **124**, 1569–1578.
55 A. Regoutz, M. Mascheck, T. Wiell, S. K. Eriksson, C. Liljenberg, K. Tetzner, B. A. D. Williamson, D. O. Scanlon and P. Palmgren, *Rev. Sci. Instrum.*, 2018, **89**, 073105.
56 B. F. Spencer, S. Maniyarasu, B. P. Reed, D. J. H. Cant, R. Ahumada-Lazo, A. G. Thomas, C. A. Muryn, M. Maschek, S. K. Eriksson, T. Wiell, T. L. Lee, S. Tougaard, A. G. Shard and W. R. Flavell, *Appl. Surf. Sci.*, 2021, **541**, 148635.
57 N. Fairley, **https://www.casaxps.com**.
58 D. J. H. Cant, B. F. Spencer, W. R. Flavell and A. G. Shard, *Surf. Interface Anal.*, 2022, **54**, 442–454.
59 G. Kresse and J. Hafner, *Phys. Rev. B: Condens. Matter Mater. Phys.*, 1993, **47**, 558–561.
60 G. Kresse and J. Hafner, *Phys. Rev. B: Condens. Matter Mater. Phys.*, 1994, **49**, 14251–14269.
61 G. Kresse and J. Furthmüller, *Phys. Rev. B: Condens. Matter Mater. Phys.*, 1996, **54**, 11169–11186.
62 G. Kresse and J. Furthmüller, *Comput. Mater. Sci.*, 1996, **6**, 15–50.
63 H. Peng, Z. H. Yang, J. P. Perdew and J. Sun, *Phys. Rev. X*, 2016, **6**, 1–15.
64 P. E. Blöchl, *Phys. Rev. B: Condens. Matter Mater. Phys.*, 1994, **50**, 17953–17979.
65 M. S. Islam and C. A. Fisher, *Chem. Soc. Rev.*, 2014, **43**, 185–204.
66 A. Urban, D.-H. Seo and G. Ceder, *npj Comput. Mater.*, 2016, **2**, 1–13.
67 A. Van Der Ven, J. Bhattacharya and A. A. Belak, *Acc. Chem. Res.*, 2013, **46**, 1216–1225.
68 R. Sharpe, R. A. House, M. J. Clarke, D. Forstermann, J. J. Marie, G. Cibin, K. J. Zhou, H. Y. Playford, P. G. Bruce and M. S. Islam, *J. Am. Chem. Soc.*, 2020, **142**, 21799–21809.
69 K. McColl, R. A. House, G. J. Rees, A. G. Squires, S. W. Coles, P. G. Bruce, B. J. Morgan and M. S. Islam, *Nat. Commun.*, 2022, **13**, 5275.